INORGANIC CHEMISTRY
FRONTIERS

RESEARCH ARTICLE

View Article Online
View Journal | View Issue

Cite this: *Inorg. Chem. Front.*, 2019, **6**, 2873

Controllable synthesis and electrochemical capacitor performance of MOF-derived MnO_x/N-doped carbon/MnO_2 composites†

Kuaibing Wang,[a] Huijian Wang,[a] Rong Bi,[a] Yang Chu,[a] Zikai Wang,[a,b] Hua Wu *[a] and Huan Pang *[c]

Received 24th May 2019,
Accepted 27th August 2019

DOI: 10.1039/c9qi00596j

rsc.li/frontiers-inorganic

A series of MnO_x/N-doped carbon/MnO_2 composites with high nitrogen amounts, namely MnO_x/NC/MnO_2, was successfully fabricated. These composites were synthesized by soaking the thermally decomposed products of Mn-MOF precursors in potassium permanganate solutions of different concentrations. The Mn-MOF precursors were constructed from the coordination of N-rich linker, 3-amino-1*H*-1,2,4-triazole-5-carboxylic acid (HATC) or pyrazine-2,3-dicarboxylic acid (H_2PDA) with Mn(II) ions. The as-synthesized composites, particularly the samples with moderate carbon/nitrogen ratios (6.76 and 1.84 for C1- and C2-based composites, respectively,) showed excellent rate capabilities, low series resistances and charge-transfer resistances as well as superior long-term cycling stabilities (more than 88% after 5000 unceasing cycles). This enhancement should be attributed to the inter-effect relationship among carbon, nitrogen and the MnO_2 layer, which gives rise to a superior synergistic-effect in minimizing ionic and electronic transmission distances, resulting in better performances.

1. Introduction

Currently, the need for fuel resources, such as oil and natural gas, has become increasingly important, resulting in a growing number of environmental issues. To achieve sustainable development, it is of significance to design and assemble advanced energy storage and conversion devices. Electrochemical capacitors (ECs), possessing higher power densities and longer endurance life than batteries, have become one of the most promising candidates.[1–3]

In order to improve the electrochemical performances of ECs, the development of new electrode materials has become a hot research area. In spite of the low conductivity, transition metal oxides (TMOs) usually exhibit a high specific capacitance and high energy density than those of carbon-based materials and conducting polymers.[4] Thus far, studies on directly using pristine TMOs, such as Co_3O_4, CuO, NiO, V_2O_5, and MnO_x, as electrode materials are still in progress.[5–10] Among them, manganese oxide is one of the most promising materials due to its rich reserve, environmental friendliness, superior electrochemical performance and low-cost.[11,12] Unfortunately, pure manganese oxide, resembling other TMOs, is poorly conductive and prone to aggregation after several charge–discharge cycles. This disadvantage factor has been a big resistance for its practical applications. Consequently, a common strategy, *i.e.*, combining with conductive carbon-based materials, was used to enhance the conductivity of the composites and thus improve the cycling performance.[13–15] However, the consistency or uniformity of the composites is still a choke point to be tackled.

Recently, a thermal decomposition method of using metal–organic frameworks (MOFs) as precursors to synthesize metal oxide/carbon composites has been found.[16,17] With the advantage of optional ligands at the molecular level, the thermal decomposition of MOFs could also obtain simply controllable porosity and a size distribution of nanomaterials with high specific surface area.[18] Few can deny that the conductivity of metal oxides are improved in the presence of carbon companions. Furthermore, different from the reported references[19,20] that have prepared the composites by physically mixing the carbon-based materials with metal oxides, the methodology of using decomposed MOFs can enhance the uniformity of metal oxide/carbon composites due to uniform MOF precursors. To date, a synergistic effect between the pyrolysis products has

[a]*Department of Chemistry, College of Sciences, Nanjing Agricultural University, Nanjing 210095, Jiangsu, P. R. China. E-mail: wuhua@njau.edu.cn*
[b]*College of Resources and Environmental Sciences, Nanjing Agricultural University, Nanjing 210095, Jiangsu, P. R. China*
[c]*School of Chemistry and Chemical Engineering, Yangzhou University, Yangzhou 225009, Jiangsu, P. R. China. E-mail: huanpangchem@hotmail.com, panghuan@yzu.edu.cn*

†Electronic supplementary information (ESI) available. See DOI: 10.1039/c9qi00596j

also been reported, which can effectively improve the resulting performances in many fields, such as photocatalysis, energy-storage and oxygen reduction reaction.[21–23] For instance, Luo *et al.*[21] found that MOF-derived ZnO/ZIF-8 hybrids displayed high catalytic activity due to the synergetic effect. Such an effect was also detected and investigated between CoNC and MoS_2 components while using them as electrocatalysts.[23]

Herein, a manganese acetate aqueous solution was selected as the metal source to react with a N-rich organic ligand, 3-amino-1*H*-1,2,4-triazole-5-carboxylic acid (HATC) or pyrazine-2,3-dicarboxylic acid (H_2PC). As a result, two Mn-based MOF precursors with controllable morphology and size were obtained by adjusting the hydrothermal reaction time. A series of amorphous compounds, *i.e.*, MnO_x/NC/MnO_2 composites with high nitrogen amounts, were further synthesized under the thermal decomposition of MOF precursors, consequently soaking the decomposed products in $KMnO_4$ solutions of various concentrations for different times. Although the soaking method in a $KMnO_4$ solution is common and simple,[24–26] reports on its influence on the nitrogen amount or the inter-effect relationship of carbon and nitrogen are scarce to date. The purposes of fabricating MnO_x/NC/MnO_2 are to consider the following aspects: (i) controlling the soaking time and the soaking concentration can adjust the proportion of carbon/MnO_2 and carbon/nitrogen of the composite; (ii) introduction of nitrogen could adjust the conductivity and enhance the wettability[27] of the electrode and consequently improve the resulting energy storage performance. In addition, the exterior structure and chemical composition of the amorphous product were also determined by SEM, EDS and XPS.

2. Experimental section

Preparation of reaction solutions

Solvents and all other chemicals (analytical grade) were purchased from commercial sources and used as received unless otherwise noted. First, 3-amino-1*H*-1,2,4-triazole-5-carboxylic acid (HATC, 3.840 g) and NaOH (1.200 g) were added into 300 mL of ultrapure water to form a 0.1 M NaATC aqueous solution. Then, for 0.1 M Na_2PDA, pyrazine-2,3-dicarboxylic acid (H_2PDA, 5.040 g) was dissolved in 300 mL of ultrapure water with the assistance of NaOH (2.400 g). Finally, a 0.5 M $Mn(OAc)_2$ solution was formed by dissolving 12.255 g of the solid product in ultrapure water (100 mL).

Synthesis of Mn-MOF precursors

To synthesize the Mn-PDA precursor, a 0.1 M Na_2PDA (90 mL) aqueous solution was added into a mixed solution of 100 mL ultrapure water and 100 mL ethanol. To disperse and decrease particle sizes, 0.1 g of polyvinylpyrrolidone (PVP) was introduced to the above system before the adding 0.5 M $Mn(OAc)_2$ (18 mL) dropwise into the solution. The mixed system was stirred for 25 min and left to react for the next 12 h. The resulting precipitate was collected by centrifugation (the speed was 14 000 rpm, for 10 min), followed by several washing cycles with water/ethanol, and finally drying in air at 50 °C for 12 h (labeled as CPP-11). The synthetic process of the Mn-ATC precursor was similar to that of CPP-11, except that the volume of $Mn(OAc)_2$ was altered to 9 mL. The resulting solid precursor was labelled as CPP-12.

Synthesis of the MnO_x/NC/MnO_2 composite

CPP-11 was placed inside a ceramic boat and was kept in a tubular furnace to decompose at 450 °C for 1 h under nitrogen atmosphere with a ramp rate of 1 °C min^{-1}. Then, the resulting calcination product (labeled as C1, 0.15 g) was soaked in $KMnO_4$ solutions of 0.01 M, 0.04 M and 0.1 M for either 45 minutes or 24 h, respectively. The final composites were obtained by centrifuging, washing and drying. The same strategy was applied on CPP-12, and the decomposed sample was named as C2. After decomposition and soaking, twelve different composites, C1-0.01 M-45 min, C1-0.04 M-45 min, C1-0.1 M-45 min, C1-0.01 M-24 h, C1-0.04 M-24 h, C1-0.1 M-24 h, C2-0.01 M-45 min, C2-0.04 M-45 min, C2-0.1 M-45 min, C2-0.01 M-24 h, C2-0.04 M-24 h, and C2-0.1 M-24 h, were synthesized, which are denoted by C1-*x*-*y* or C2-*x*-*y* for convenient description, where *x* represents the concentration of the $KMnO_4$ solution and *y* is the soaking time.

Fabrication of the working electrode

Three-electrode system: acetylene black (15 mg) and the as-synthesized active material (80 mg) were mixed by grinding. Then, the mixture was introduced into an isopropanol system, containing PTFE (5 mg) and continuously stirred until the complex was distributed uniformly. Nickel foam (size: 1 cm × 5 cm) was chosen due to its porosity and large contact area, and it was washed with ethanol several times. The slurry was loaded onto nickel foam (area: 1 cm × 1 cm) and it was pressed by a manual rolling press (MR-100A, MTI Corp.). Notably, the loading mass ranged in 2.4–6.2 mg. The two electrode system was modified following a recent reference.[28]

Methods and measurements

X-ray photoelectron spectroscopy (XPS), using nonmonochromatized $Al_{K\alpha}$ X-ray as the excitation source, was performed on an ESCALab MKII X-ray photoelectron spectrometer. X-ray powder diffraction (XRD) data were recorded on a Bruker D8 Advance instrument using $Cu_{K\alpha}$ radiation (λ = 1.54056 Å) at room temperature. The morphology of the as-synthesized hybrid products were obtained by using a Hitachi S-4800 field-emission scanning electron microscope (FE-SEM). The corresponding energy dispersive X-ray (EDS) spectroscopy data for oxide samples were obtained on a JEOL JSM-7500F scanning electron microscope. The adsorption–desorption isotherms of nitrogen were measured using a V-Sorb 2800P adsorption equipment (Gold APP Instrument, Beijing, China). All electrochemical measurements (cyclic voltammetry (CV) and chronopotentiometry (CP)) were performed on an electrochemical analyzer system, CHI660E (Chenhua Instrument, Shanghai, China), in a three-electrode cell that included a platinum wire

counter electrode, a saturated calomel electrode (SCE) as the reference electrode and a working electrode. The electrolyte was a Na_2SO_4 aqueous solution (0.5 M). Electrochemical impedance spectroscopy (EIS) measurements of the as-synthesized samples were conducted at an open circuit voltage in the frequency range of 100 kHz to 10 mHz. The conductivity data of the solid samples were obtained with four-point probes.

3. Results and discussion

Samples C1 and C2 were synthesized through the decomposition of Mn-based MOF precursors of CPP-11 and CPP-12, respectively. The chemical composition of C1 and C2 was first characterized by XRD (Fig. 1a), and the results show the weak intensities of diffraction peaks, indicating the low crystallinity of the composites, which can be well-indexed to the standard values for Mn_3O_4 that is a tetragonal spinel structure (JCPDS No. 24-0734). In a bid to further investigate the reason for low crystallinity, XPS and EDS analyses were also implemented. The oxidation state of manganese was further confirmed by the splitting patterns within the Mn 2p region. The splitting width is 11.70 eV (Fig. 1b), which is in good accordance with the recent reports on Mn_3O_4.[29] The deconvolution of C 1s and N 1s peaks illustrates the presence of high amounts of carbon and nitrogen inherited from the N-rich organic linker, which would be a possible reason for the low crystallinity (Fig. 1c and d). Particularly, high amounts of amorphous carbon might wrap up or cover the surface of Mn_3O_4, thus influencing the crystallinity. Keeping up with its mother precursor, C1 product possessed a higher carbon amount (At%: 40.34) and a lower nitrogen amount (At%: 17.92) than C2 sample (C%: 36.84; N%: 24.19). This result indicates that decomposing a MOF-based precursor is a good methodology for producing high N-doped inorganic materials.[30] Besides, there exists a large number of functional groups, such as C=O or C–N, which are covalently bonded with each other in the internal structure. Actually, the chemical composition of C1 or C2 sample can be deduced as Mn_3O_4/N-doped carbon (simplified as Mn_3O_4/NC). In addition, EDS analyses confirmed the presence of carbon, nitrogen, oxygen and manganese in these hybrid materials (Fig. S1†), indicating that whether sample C1 or C2 consisted of manganese oxides and N-doped amorphous carbon.

SEM images display that both C1 and C2 have rod-type structures, as shown in Fig. 2. Due to different coordination modes and environments of their coordination polymer precursors, their detailed structures vary accordingly. Sample C1 consists of micrometer-sized rods and a great number of nanoparticles (20 nm) attached to the surface of rods. However, for sample C2, the components of carbon and Mn_3O_4 were heavily integrated with each other to assemble a rod-like unity with a porous surface. Moreover, the length of a C2 rod is shorter than that of a C1 rod, while sample C2 possesses thick layers resembling a tetragonal bulk-rod.

The target composites, MnO_x/NC/MnO_2, were obtained by soaking the decomposed product, Mn_3O_4/NC, in a $KMnO_4$

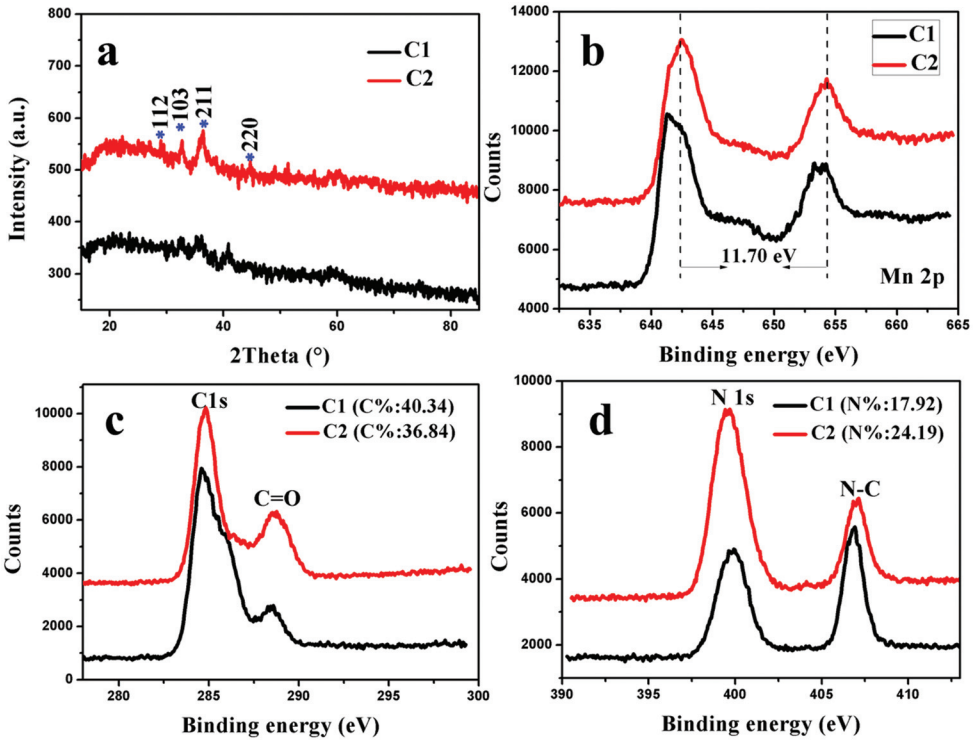

Fig. 1 Structural characterization. (a) XRD patterns of C1 and C2 samples. (b–d) The XPS spectra of Mn 2p, C1s and N 1s regions of MOF-derived C1 and C2 samples.

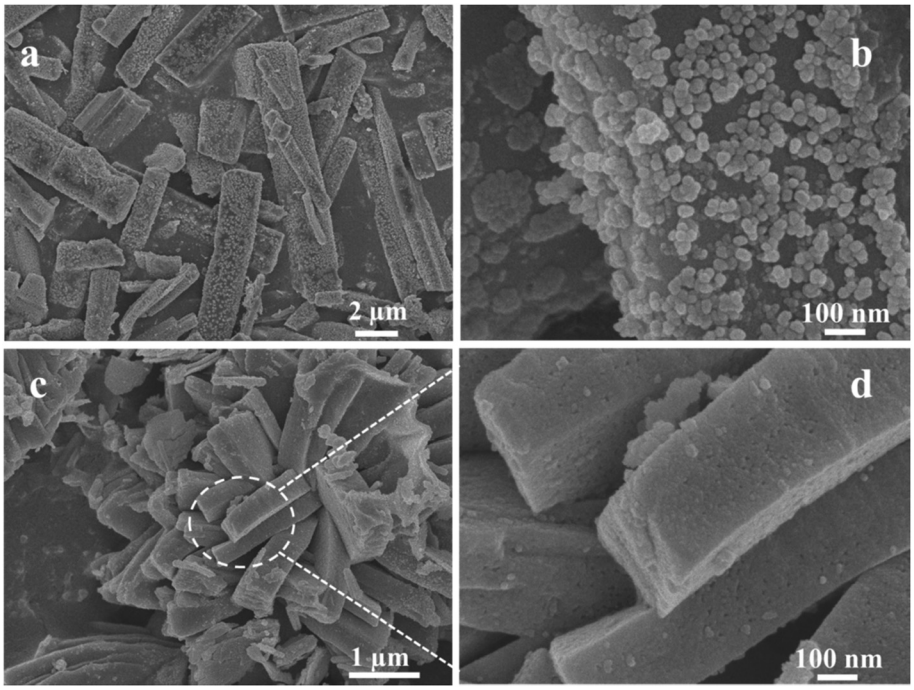

Fig. 2 Morphology characterization. (a–b) SEM images of the MOF-derived C1 product. (c–d) SEM images of MOF-derived C2 bulk-rods.

solution. After adjusting the soaking time and the concentration of the solution, a series of composites were obtained, which are denoted as C1-*x*-*y* and C2-*x*-*y* for convenient description (detailed information can be seen in the Experimental section). For C1-*x*-*y*, by fixing the soaking time at 45 min, the mean size of the particles on the surface increased from 40 nm, 100 nm to larger gathering motifs with the rise in the concentration of the $KMnO_4$ solution from 0.01, 0.04 to 0.1 M, respectively (Fig. 3).

When the soaking time was increased up to 24 h, massive particles with larger sizes were obtained, particularly at higher concentrations of the $KMnO_4$ solution (Fig. 4). The increase in the size can confirm the oxidizing influence of $KMnO_4$. More importantly, whether the reaction system underwent a short-time soaking period or a long-term soaking, there existed abundant particles with a mean size of several nanometers on the surface, which could be recognized as the generated MnO_2 species due to the reaction between amorphous carbon and $KMnO_4$. The detailed synthesis procedure can be described according to reaction (1):[31]

$$4KMnO_4 + 3C + H_2O = 4MnO_2 + 2KHCO_3 + K_2CO_3 \quad (1)$$

To elucidate the above deduction and the components of these composites after soaking, XPS analysis was further carried out after XRD analyses to confirm that all the composites after soaking were amorphous due to the rapid precipitation and the wrapping of MnO_2. Fast nucleation, followed by aggregation and fusion will not facilitate the formation of crystalline samples in the absence of further growth and annealing.[32] As shown in Fig. 5, within the survey region (0–1350 eV), carbon, oxygen, nitrogen and manganese species were detected both in C1-*x*-*y* or C2-*x*-*y*, which is consistent with EDS data (Fig. S3 and S4†). The deconvolution of the Mn 2p peak suggests several other peaks centered at 641.6–641.9 eV and 642.8 eV except for the two main peaks that are ascribed to Mn $2p_{1/2}$ and Mn $2p_{3/2}$ of Mn_3O_4 (Fig. S5a†). The binding energy (BE) values ranging 641.6–641.9 eV correspond to Mn_2O_3 species (641.7 eV for C1-*x*-*y*, 641.8 eV for C2-*x*-*y*) that could originate from the further oxidation of Mn_3O_4 through potassium permanganate.[33] This result suggests that $KMnO_4$ can also react or influence the Mn_3O_4 within the period of reaction (1). The partial oxidation of Mn_3O_4 can confirm the point that Mn_3O_4 cores are wrapped up or covered in N-doped carbon. As for 642.8 eV, it can be attributed to MnO_2 species.[34] Therefore, MnO_2 is the product from the reaction between amorphous carbon and potassium permanganate, which confirms the above deduction. Similarly, C2-*x*-*y*-based products have similar peaks centered approximately at 641.8 eV and 642.8 eV, corresponding to Mn_2O_3 and MnO_2, respectively (Fig. S5b†).

Moreover, comparison analyses of the atomic content of Mn, C and N elements before and after the soaking procedure can also illustrate the occurrence of the oxidation reaction. As shown in Table 1, two important findings can be concluded: (i) in comparison to the C1 product, the content of carbon of the samples decreased, while that of Mn increased sharply after soaking, indicating the oxidation reaction between the carbon layer and the $KMnO_4$ solution; (ii) the longer the soaking time or the larger the soaking concentration, the higher the amount of Mn and the lower the amount of carbon. Similar results were observed for C2-based samples, as clearly depicted in Table S1.† In comparison to the carbon layer, the

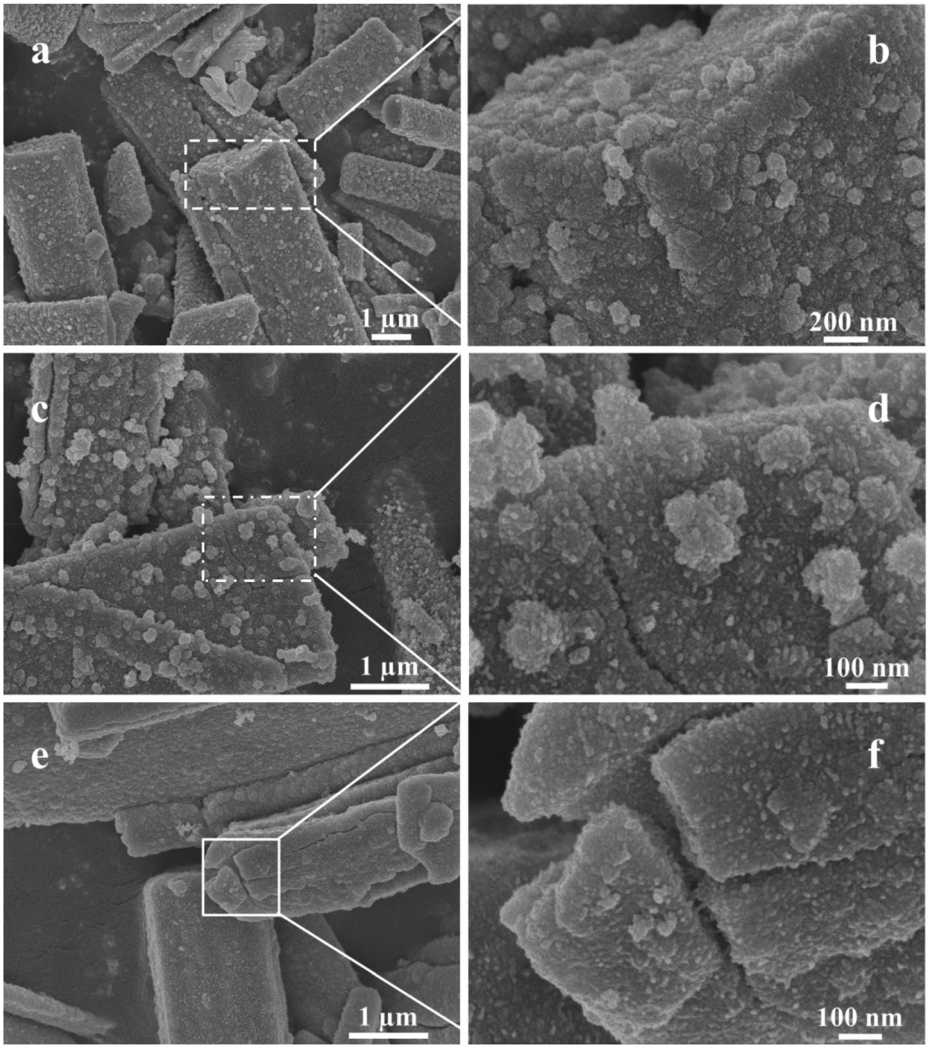

Fig. 3 Morphology characterization of C1-*x*-45 min samples. (a–b) SEM images of the C1-0.01 M-45 min sample. (c–d) SEM images of the C1-0.04 M-45 min sample. (e–f) SEM images of the C1-0.10 M-45 min sample.

influence of the soaking procedure on the nitrogen component not only displayed a similar variation trend but also showed a more intense tendency. For example, the carbon retention even after soaking in 0.1 M $KMnO_4$ for 24 h maintanined around 50% for both the C1 and C2 samples. However, under same conditions, nitrogen retentions were 14% and 31% for C1 and C2 samples, respectively. Moreover, the as-obtained nitrogen amount of the soaked product was much higher than that of the reported references that used different approaches (see Table 2 and Table S2† for details).[35–39] Therefore, soaking in $KMnO_4$ with various concentrations can not only result in different carbon contents and thicknesses of the MnO_2 layer but can also have an effect on the final amount of nitrogen.

Cyclic voltammetry (CV) and chronopotentiometry (CP) measurements were implemented to investigate the potential electrochemical performance of the target products (C1-*x*-*y* or C2-*x*-*y*). Fig. 6 and Fig. S6† show the CV curves of C1-*x*-*y* and C2-*x*-*y* at different scan rates in a potential span of 0–0.8 V. As depicted, all the CV curves exhibit nearly rectangular shapes and no obvious redox peaks, which resemble the pristine MnO_2 electrode mentioned in published reports.[40] The electrochemical behaviors of all the composites belong to the pseudo-capacitive character, which relies on the insertion/deinsertion of K^+ at or near the surface of the MnO_2 layer.[40] The detailed faradaic reaction can be described as follows:

$$MnO_2\text{-layer} + K^+ + e^- \leftrightarrow MnOOK \quad (2)$$

The specific capacitance values determined from the CV curves of C1-0.04 M-24 h and C2-0.04 M-24 h, 384.8 and 392.3 F g^{-1}, respectively, at a scan rate of 5 mV s^{-1}, are apparently much larger than those of the other samples. Detailed capacitances *versus* scan rates are depicted in Fig. S7.† It suggests that a moderate erosion concentration and a long-period immersion are beneficial for improving the electrochemical performance. When the immersion concentration stays at a low level (0.01 M or 0.04 M), the sample shows better electro-

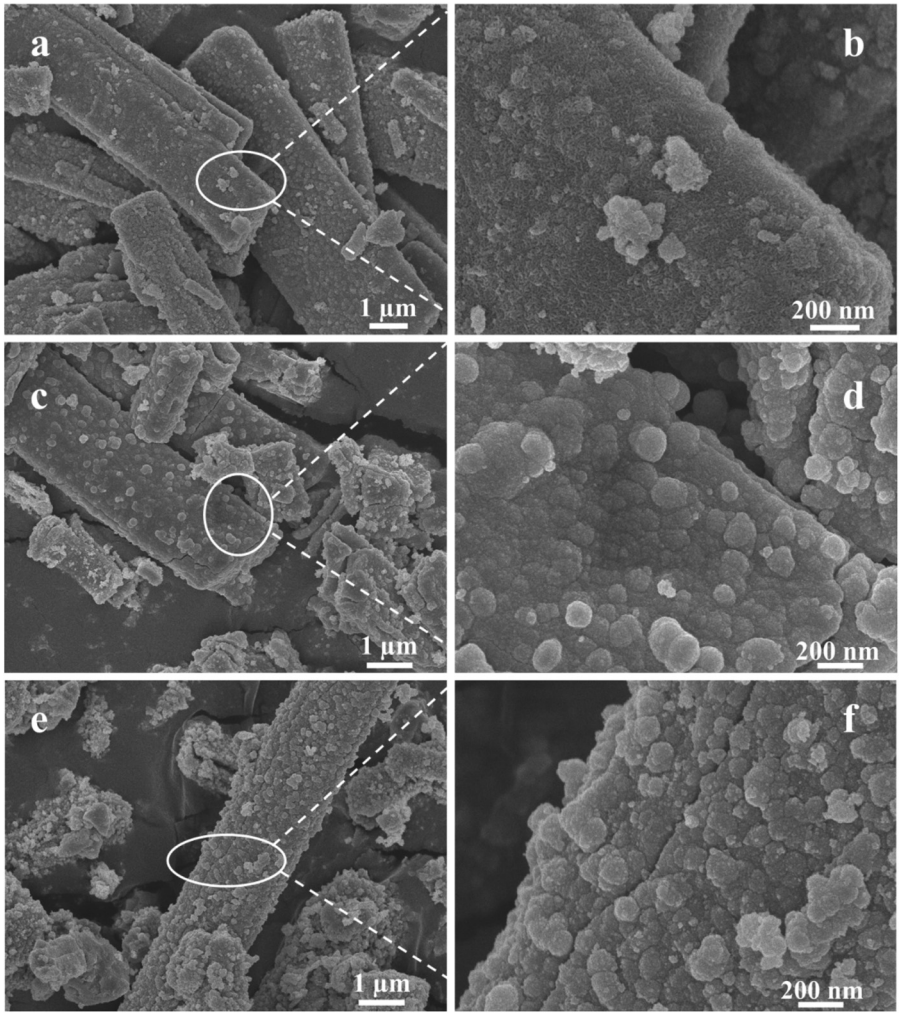

Fig. 4 Morphology characterization of C1-*x*-24 h samples. (a–b) SEM images of the C1-0.01 M-24 h sample. (c–d) SEM images of the C1-0.04 M-24 h sample. (e–f) SEM images of the C1-0.10 M-24 h sample.

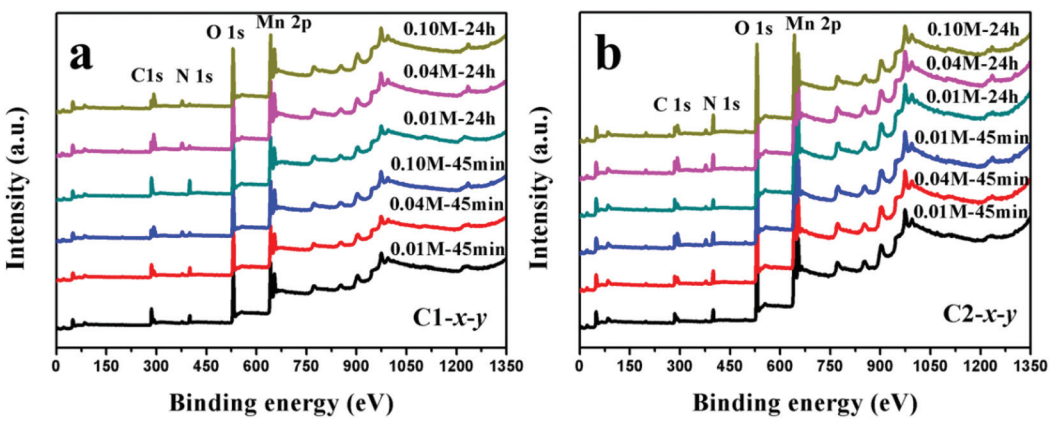

Fig. 5 Structural characterization of C-*x*-*y* samples. (a) Survey scan XPS patterns of C1-*x*-*y* samples. (b) Survey scan XPS patterns of C2-*x*-*y* samples.

chemical performance after long-time soaking. When the concentration was increased up to 0.1 M, the capacitance of the sample with a soaking time of 45 min was larger than that of the sample immersed for 24 h, regardless of the sample C1 or C2. This result indicates that a high concentration easily generates the rapid nucleation of the MnO_2 layer and thus gives rise

Table 1 The content of Mn and C of C1-*x*-*y* obtained from XPS spectra

	Element (atomic concentration %)	
Samples	Mn	C
C1	5.66	40.34
C1-0.01 M-45 min	14.78	35.95
C1-0.04 M-45 min	17.28	33.32
C1-0.10 M-45 min	22.62	25.40
C1-0.01 M-24 h	17.19	33.79
C1-0.04 M-24 h	23.22	23.69
C1-0.10 M-24 h	25.94	20.54

to more exterior redox sites against ion insertion. Therefore, the depletion of carbon and nitrogen and the MnO_2 layer would change the relative proportions of conductive and non-conductive materials in the composite. As a result, a moderate erosion concentration and long-period immersion can generate a more reasonable C/N/MnO_2 proportion and more exterior redox sites.

Capacitive data obtained from CP methods are in good accordance with those obtained from the CV methodology. The detailed CP measurements for MnO_x/NC/MnO_2 products are depicted within a 0–0.8 V potential window, as shown in Fig. 7 and S8.† Similarly, the specific capacitance values for electrodes C1-0.04 M-24 h and C2-0.04 M-24 h were calculated from the discharging times of 280.8 and 284.9 F g^{-1} at a current density of 0.125 A g^{-1}, respectively, which were also higher than those of the other electrodes. In contrast, the capacitance of the C1-0.04 M-24 h (or C2-0.04 M-24 h) electrode is two or three times larger than that of the pristine C1 (or C2) electrode, as depicted in Fig. S9.† The gravimetric capacitance values of C1 and C2 electrodes are 92 and 128 F g^{-1} at 0.125 A g^{-1}, respectively. This result indicates that the morphological discrepancies before and after soaking may be the key factor for different electrochemical performances. Alternation of morphology should affect the resulting surface area and BET gas-sorption measurements, as shown in Fig. S10.† As a result, the BET specific surface areas for C1, C2, C1-0.04 M-24 h and C2-0.04 M-24 h were 8.4, 9.9, 30.7 and 63.1 m^2 g^{-1}, respectively. This indicates that $KMnO_4$ soaking substantially enhances the surface area of C1- and C2-based samples, thus improving their final properties.

In addition to the morphology and surface area, the proportion of carbon/MnO_2, content of carbon and nitrogen and the diffusion distance as well as the synergistic effect of all these factors affect the transfer rate of electrolyte ions and electrons, consequently influencing the resulting performances. It is hard to detect the thickness of the MnO_2 layer, and thus the proportions of carbon and nitrogen are listed in Table S3† to illustrate the possible synergistic effects. Taking the C1-based electrode for example, especially for C1-0.04 M-45 min and C1-0.04 M-24 h, C/N ratio for both were centered in the middle position (3.90 and 6.76, respectively), and they consequently displayed larger specific capacitances than those of the other electrodes (as shown in Fig. S7a†). The middle position means both carbon and nitrogen contents lie in a low mediate level based on the results of Tables 1 and 2. Moreover, the low amounts of carbon and nitrogen suggest the generation of high MnO_2 contents during the soaking procedure. Interestingly, C1-0.10 M-45 min and C1-0.10 M-24 h electrodes (possessing higher C/N ratio) with higher MnO_2 amounts generate worse electrochemical performances. The possible reason for this phenomenon is that an excessive MnO_2 content may cover the surface of carbon and nitrogen, thus hindering their roles. The possible roles are that a moderate amount of carbon may provide a good conductivity and an appropriate concentration of nitrogen-doping could further enhance the conductivity of the composites. Detailed conductivity data measured by a four-point probe could confirm this opinion (Table S4†). The result suggests a lower carbon amount, a moderate nitrogen content and an appropriate amount of the MnO_2 layer can reach a superior synergy and the corresponding composite possesses a more excellent conductivity. Therefore, a certain kind of relationship should exist between the content ratio of carbon and nitrogen as well as the MnO_2 layer according to conductivity data.

When the performances of C1 and C2 electrodes were compared, C2 showed better electrochemical performances in some aspects, such as a higher capacitance and a superior rate capability. The detailed specific capacitances *versus* current densities are listed in Fig. S11.† The gravimetric capacitance values for C1-0.04 M-24 h and C2-0.04 M-24 h were calculated to be 280.8, 245.8, 221.3, 206.9, 192.2 F g^{-1} and 284.9, 273.1, 264.6, 244.7, 229.4 F g^{-1} at the current densities of 0.125, 0.25, 0.625, 1.25 and 2.50 A g^{-1}, respectively. The electrochemical data can be compared with the recent references on MnO_2-based SC electrode materials (Table S5†), such as MnO_2/CNF

Table 2 The content of nitrogen obtained from XPS spectra

Samples	Nitrogen (atomic concentration %)	Samples	Nitrogen (atomic concentration %)
C1-0.01 M-45 min	12.11	C2-0.01 M-45 min	14.79
C1-0.04 M-45 min	8.53	C2-0.04 M-45 min	10.80
C1-0.10 M-45 min	5.07	C2-0.10 M-45 min	10.19
C1-0.01 M-24 h	8.54	C2-0.01 M-24 h	12.04
C1-0.04 M-24 h	3.50	C2-0.04 M-24 h	10.62
C1-0.10 M-24 h	2.58	C2-0.10 M-24 h	7.60
C1	17.92	C2	24.19

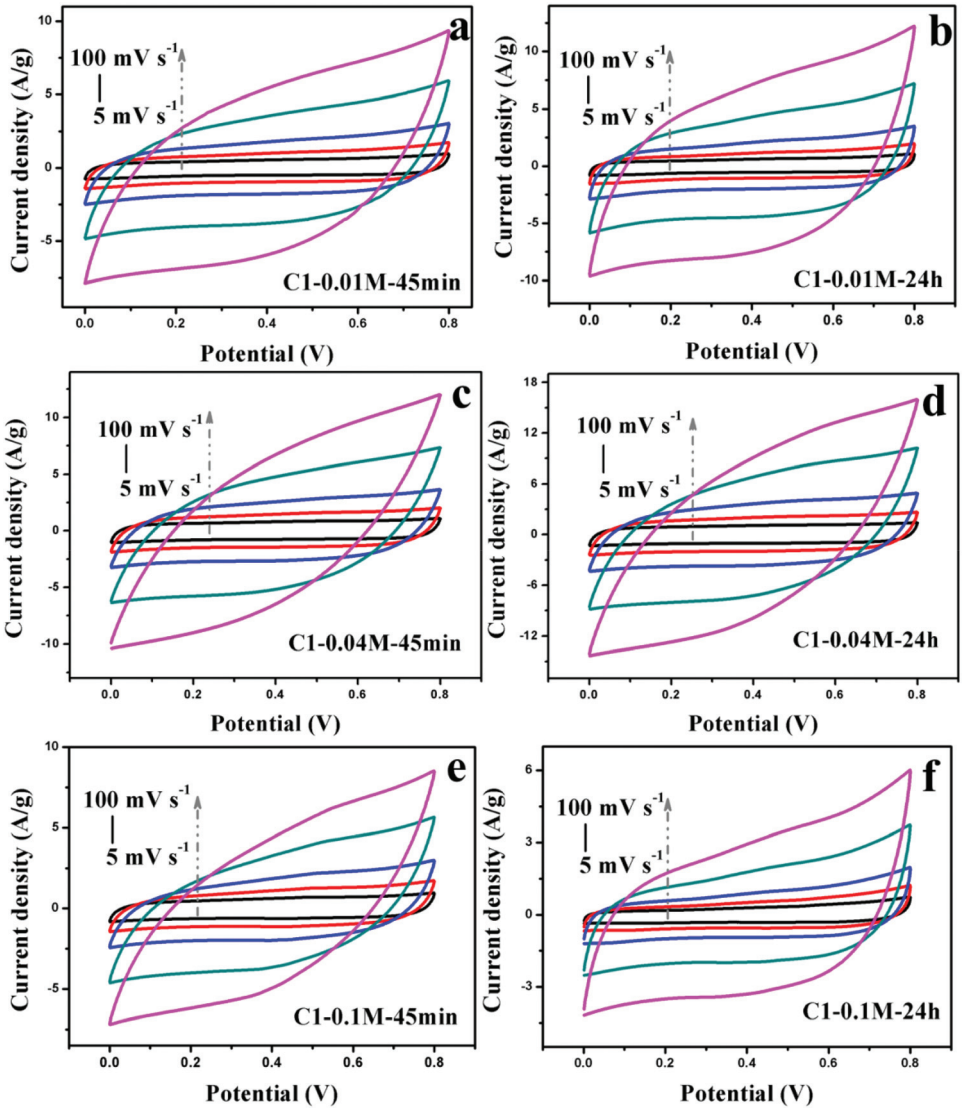

Fig. 6 Electrochemical performance. (a–b) CV curves of the as-synthesized C1-0.01 M-*y* electrodes at different scan rates. (c–d) CV curves of the as-synthesized C1-0.04 M-*y* electrodes at different scan rates. (e–f) CV curves of the as-synthesized C1-0.10 M-*y* electrodes at different scan rates.

(321.3 F g^{-1} at 1.0 A g^{-1}), MnO_2 NAs/GO (maximum: 152.5 F g^{-1}), MnO_2/mesoporous carbon (maximum: 326 F g^{-1}) and so forth.[41–49]

It is noteworthy to mention that the C2-0.04 M-24 h electrode (80.5% remained) still retained a more superior rate capability after a 20-fold increase in current density, compared to the C1-0.04 M-24 h electrode (68.5% remained). Moreover, the other electrodes almost displayed similar trends as that of the C2 electrode, possessessing more excellent rate capabilities (Table S6†). This may be due to the higher nitrogen amount in the C2 electrode, which was inherited from the nitrogen-rich mother precursors at first. A high nitrogen atom content can facilitate the fast transmission of ions and electrons and increase the wettability of the electrode material itself, consequently improving the resulting electrochemical properties. This deduction can be proved by the detailed XPS experimental data shown in Table 2, which indicate that C2 samples possess a higher content of nitrogen atoms than C1 products in general.

Second, the fast delivery of electrons and ions in the C2 electrode may be due to the lower series resistance (R_s, including the bulk-solution resistance, the contact resistance, *etc.*) and charge-transfer resistance (R_{ct}). The electrical resistance is an important evaluation parameter for SC electrode, which has been quantitatively determined by electrochemical impedance spectroscopy (EIS) over the frequency range of 100 kHz-10 mHz, as shown in Fig. 8. In general, the Nyquist plots of C1 and C2 electrodes have similar patterns that are composed of one semicircle in the high frequency region (dominated by kinetic control) and a straight line in the low frequency region (related to diffusion control).[50] By calculating and modulating *via* the ZView software, the EIS data could be well fitted to an equivalent circuit, as shown in the inset of Fig. 8. Both the C1-

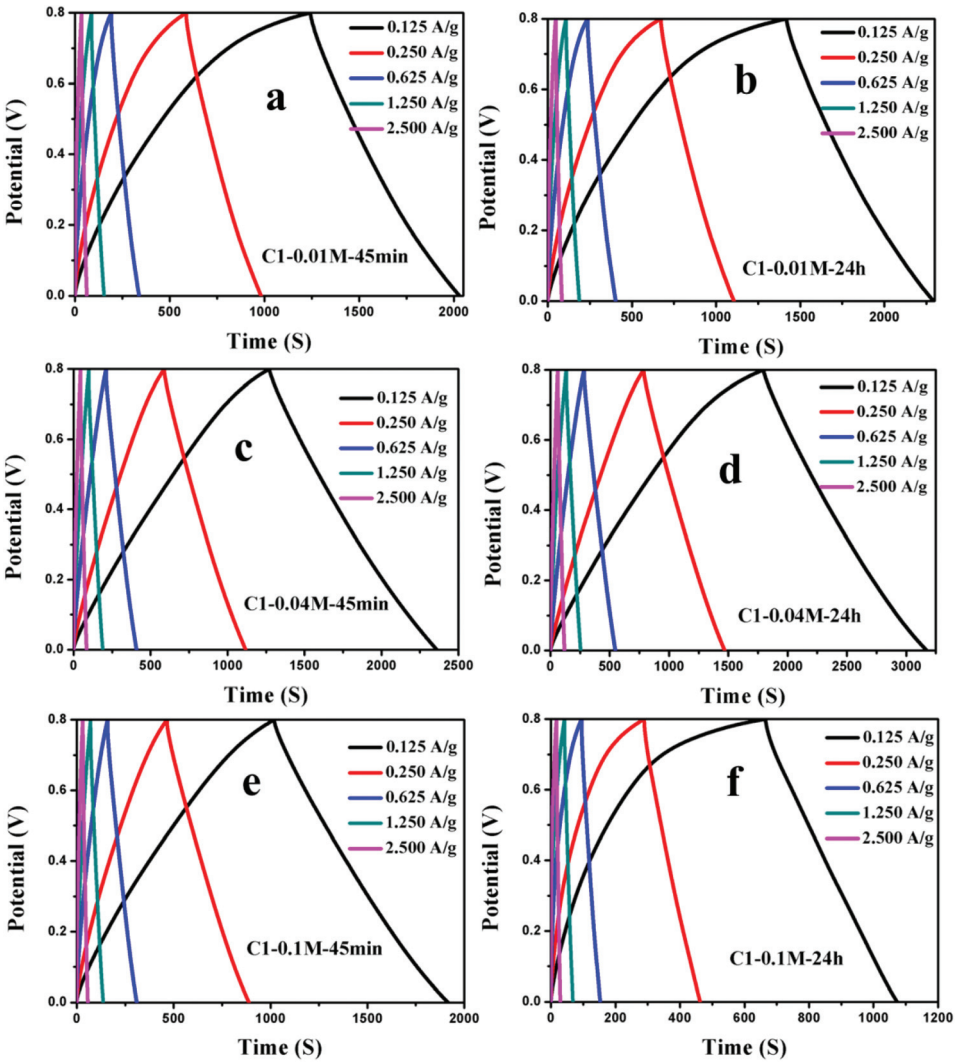

Fig. 7 Charge–discharge curves. (a–b) CP curves of the as-synthesized C1-0.01 M-*y* electrodes at different current densities. (c–d) CP curves of the as-synthesized C1-0.04 M-*y* electrodes at different current densities. (e–f) CP curves of the as-synthesized C1-0.10 M-*y* electrodes at different current densities.

0.04 M-24 h and C2-0.04 M-24 h electrodes have lower R_s and R_{ct} values in comparison to other electrodes. Among them, C1-0.1 M-24 h and C2-0.1 M-24 h electrodes possess the highest R_s and R_{ct} values and these results are in accordance with the CV and CP analyses. The R_s values for C1-0.04 M-24 h and C2-0.04 M-24 h calculated from the points intersecting the Z' axis (real axis) were 1.97 and 1.94 Ω, respectively. Moreover, the corresponding R_{ct} values determined and simulated from the ZView software were about 5.93 and 5.57 Ω. The detailed EIS data for the other electrodes are listed in Table S7,† which confirm that the lower concentration and the long-period soaking are the superior conditions for the synthesis of composite electrodes. These observations also manifest that the electrode with lower R_s and R_{ct} values has more affinity towards the surface insertion/deinsertion reaction.

Based on the above-mentioned traits of these electrodes, the cycling stability, which is another vital parameter for evaluating SC electrodes, was studied using CV methodology (100 mV s^{-1}) to examine the two superior electrodes (C1-0.04 M-24 h and C2-0.04 M-24 h). As shown in Fig. S12,† regardless of the C1-0.04 M-24 h or the C2-0.04 M-24 h electrode, the specific capacitance grows larger even after 1600 continuous cycles and decreases slightly over the rest of the 3400 cycles. After 5000 unceasing cycles, the capacitance retentions for C1-0.04 M-24 h and C2-0.04 M-24 h were 88.9% and 89.5%, respectively, suggesting the superior cycling stability of the composite electrodes. The upward tendency of capacitance before 1600 cycles may be due to the activation and the infiltration process, which requires a period of time to penetrate between the active material and the electrolyte. The difference between C1-0.04 M-24 h and C2-0.04 M-24 h electrodes occurs before 1200 cycles. The capacitance remains at a stable level after 300 cycles for the C1-0.04 M-24 h electrode, while there is a gradually increasing trend within 1200 cycles for C2-0.04

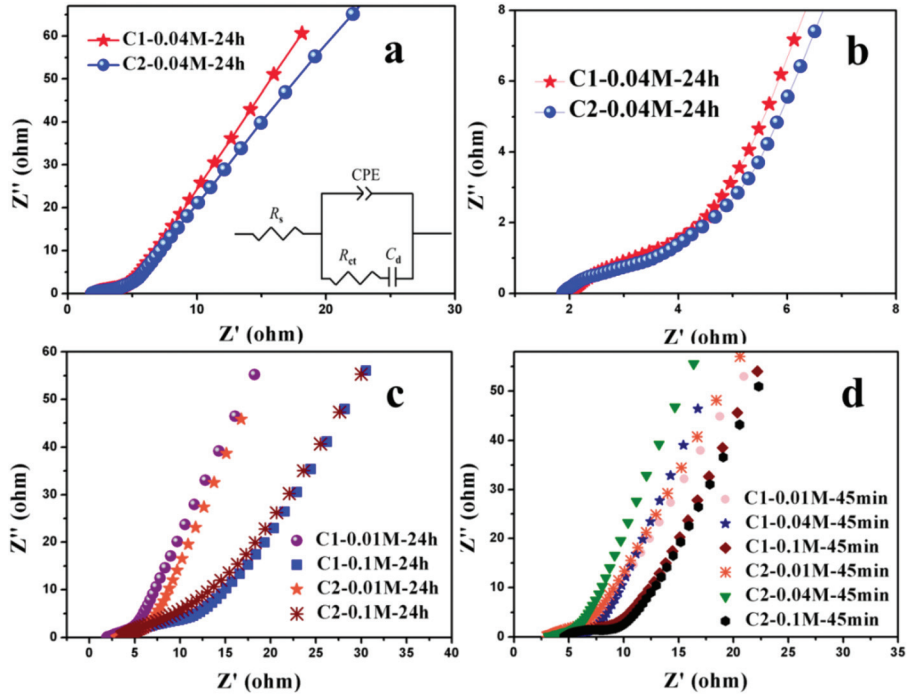

Fig. 8 Electrochemical impedance spectra. (a) Nyquist plots of the as-prepared C1-0.04 M-24 h and C2-0.04 M-24 h hybrid electrodes at room temperature; inset shows an equivalent circuit. (b) A magnification image of EIS data. (c–d) Nyquist plots of other hybrid electrodes.

M-24 h. This phenomenon may be also ascribed to different nitrogen contents that cause various electrode wettabilities, resulting in different activation processes of the electrode.

Two asymmetric supercapacitor (ASC) devices were further assembled by employing C1-0.04 M-24 h (or C2-0.04 M-24 h) as the positive electrode and active carbon (AC) as the negative

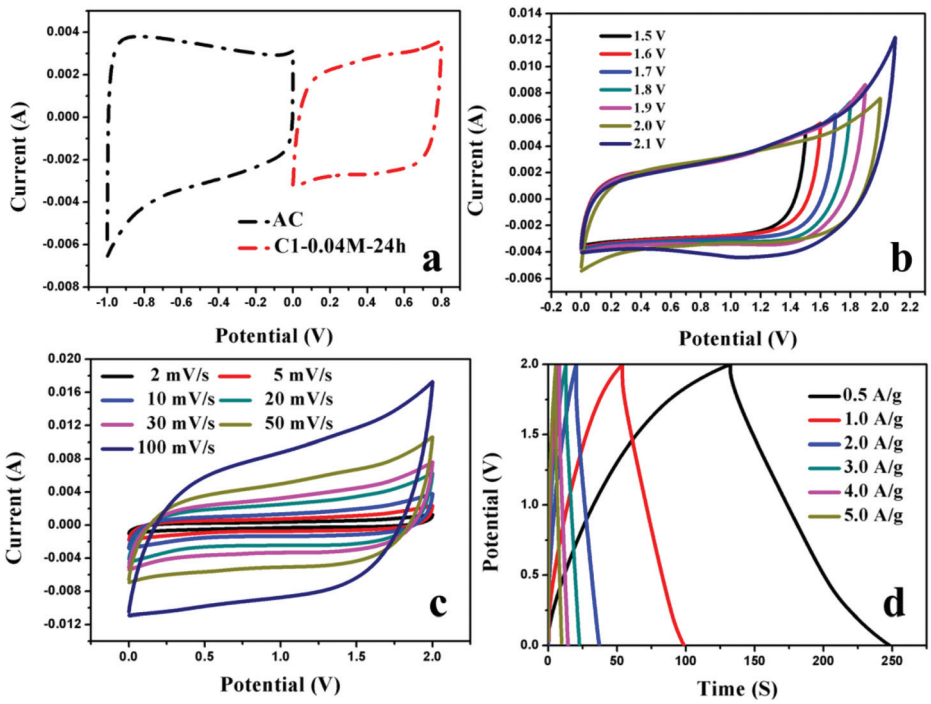

Fig. 9 CV curves of (a) C1-0.04 M-24 h and AC at a sweep rate of 10 mV s^{-1}, (b) C1-0.04 M-24 h//AC ASC device ranged in a different potential window at a scan rate of 30 mV s^{-1}. (c) CV curves of C1-0.04 M-24 h//AC ASC device at different sweep rates. (d) CP curves of C1-0.04 M-24 h//AC ASC device at different current densities.

electrode. The gravimetric capacitance of AC, as shown in Fig. S13,† was determined to be 131 F g^{-1} in the potential range of −1.0 to 0 V. Therefore, the working voltage of the assembled C1-0.04 M-24 h//AC or C2-0.04 M-24 h//AC ASC device is expected to achieve 1.8 V (Fig. 9a). Based on the distorted situations of the CV curves at different voltage windows, an operating voltage of 2.0 V was finally selected, as shown in Fig. 9b (Fig. S14a†). No apparent distortions of the CV curves were observed with a sweep rate increase from 2.0 to 100 mV s^{-1}, illustrating the good reversibility and excellent capacitive behavior of the as-obtained ASC devices within such a potential window (Fig. 9c and S14b†).[51]

The ASC devices of C1-0.04 M-24 h//AC and C2-0.04 M-24 h//AC obtained gravimetric capacitances of 29.0 and 30.1 F g^{-1} at a current density of 0.5 A g^{-1}, respectively (Fig. 9d and S14c†). Even after 2000 continuous charge–discharge measurements, the capacitance retentions remained at 86.2% and 85.8% for C1-0.04 M-24 h//AC and C2-0.04 M-24 h//AC, respectively, indicating their superior cycling stabilities (Fig. S15†). Although the specific capacitances were not high enough, the ASC device still displayed a maximum energy density of 16.8 W h kg^{-1} at a power density of 499 W kg^{-1} due to the high operating potential window (Fig. S14d†). The as-obtained energy value is comparable to or even higher than that of MnO_2-based or AC-based ASC devices in recent reports, such as MnO_2//AC (12.8 W h kg^{-1} at 2197 W kg^{-1}),[52] Fe-MnO_2//AC (20.2 W h kg^{-1} at 225 W kg^{-1}),[53] CNT@PPy@MnO_2//AC (38.42 W h kg^{-1} at 100 W kg^{-1}),[54] Co_9S_8/NS-C//AC (14.85 W h kg^{-1} at 681.82 W kg^{-1}),[55] and so forth, suggesting that the oxides/NC@MnO_2 electrode can be a good candidate for practical applications in energy-storage fields.

4. Conclusion

In summary, a series of MnO_x/NC/MnO_2 samples with controllable carbon/nitrogen ratio was synthesized by soaking Mn-MOF-derived Mn_3O_4/NC rods in $KMnO_4$ solutions with varying concentrations for varying soaking times. The decorated rod-like composites were directly evaluated as SC electrode materials. The results suggest that different soaking times and soaking concentrations not only result in different amounts of carbon and MnO_2, but also affect the nitrogen content of these composites, consequently influencing the ratio among carbon, nitrogen and the MnO_2 layer, which can further influence the resulting electrochemical performances. In contrast, the composite soaked in 0.04 M $KMnO_4$ for 24 h, particularly the C2 sample, showed an excellent rate capability (80.5% remained after a 20 times increase in current density), a low series resistance (1.94 Ω) and a charge-transfer resistance (5.57 Ω) and a superior long-term cycling stability (more than 88% after 5000 unceasing cycles). It is believed that such oxides/NC@MnO_2 materials with controllable amounts of nitrogen and carbon can be facilely synthesized based on this soaking methodology, and these materials can serve as promising candidates for applications in other fields.

Conflicts of interest

There are no conflicts to declare.

Acknowledgements

This work was supported by the Qing Lan Project of Jiangsu Province, the Natural Science Foundation of Jiangsu Province (BK20180514, BK20131314), the National Natural Science Foundation of China (21371098), the China Postdoctoral Science Foundation (2015M570430), the Jiangsu Postdoctoral Science Foundation (1401007C) and the Scientific Research Foundation of Nanjing Agricultural University (050804087).

References

1 (*a*) J. Yan, Q. Wang, T. Wei and Z. J. Fan, *Adv. Energy Mater.*, 2014, **4**, 1300816; (*b*) F. Wang, X. Wu, X. Yuan, Z. Liu, Y. Zhang, L. Fu, Y. Zhu, Q. Zhou, Y. Wu and W. Huang, *Chem. Soc. Rev.*, 2017, **46**, 6816.
2 Z. Wu, L. Li, J. M. Yan and X. B. Zhang, *Adv. Sci.*, 2017, **4**, 1600382.
3 M. Salanne, B. Rotenberg, K. Naoi, K. Kaneko, P. L. Taberna, C. P. Grey, B. Dunn and P. Simon, *Nat. Energy*, 2016, **1**, 16070.
4 (*a*) Z. Niu, H. Dong, B. Zhou, J. Li, H. Hng, W. Zhou, X. Chen and S. Xie, *Adv. Mater.*, 2013, **25**, 1058; (*b*) T. Lv, M. Liu, D. Zhu, L. Gan and T. Chen, *Adv. Mater.*, 2018, **30**, 1705489; (*c*) K. Wang, H. Wu, Y. Meng and Z. Wei, *Small*, 2014, **10**, 14.
5 (*a*) M. Zhang, H. Fan, N. Zhao, H. Peng, X. Ren, W. Wang, H. Li, G. Chen, Y. Zhu, X. Jiang and P. Wu, *Chem. Eng. J.*, 2018, **347**, 291; (*b*) M. Huang, Y. Zhang, F. Li, L. Zhang, Z. Wen and Q. Liu, *J. Power Sources*, 2014, **252**, 98.
6 Y. Zhang, M. Kuang and J. Wang, *CrystEngComm*, 2019, **16**, 492.
7 (*a*) X. Wang, K. Cao, Y. Wang and L. Jiao, *Small*, 2017, **13**, 1700873; (*b*) Z. Ma, K. Rui, Q. Zhang, Y. Zhang, M. Du, D. Li, Q. Wang, X. Huang, J. Zhu and W. Huang, *Small*, 2017, **13**, 1603500.
8 J. Lin, H. Jia, H. Liang, S. Chen, Y. Cai, J. Qi, C. Qu, J. Cao, W. Fei and J. Feng, *Adv. Sci.*, 2018, **5**, 1700687.
9 (*a*) H. Lai, Q. Wu, J. Zhao, L. Shang, H. Li, R. Chen, Z. Lyu, J. Xiong, L. Yang, X. Wang and Z. Hu, *Energy Environ. Sci.*, 2016, **9**, 2053; (*b*) N. Chodankar, S. Selvaraj, S. H. Ji, Y. Kwon and D. H. Kim, *Small*, 2019, **15**, 1901145.
10 (*a*) N. Jabeen, A. Hussain, Q. Xia, S. Sun, J. Zhu and H. Xia, *Adv. Mater.*, 2017, **29**, 1700804; (*b*) L. Liu, L. Su, J. Lang, B. Hu, S. Xu and X. Yan, *J. Mater. Chem. A*, 2017, **5**, 5523.
11 S. Faraji and F. N. Ani, *J. Power Sources*, 2014, **263**, 338.
12 G. Zhang, X. Xiao, B. Li, P. Gu, H. Xue and H. Pang, *J. Mater. Chem. A*, 2017, **5**, 8155.
13 M. Zhi, C. Xiang, J. Li, M. Li and N. Wu, *Nanoscale*, 2013, **5**, 72.

14 X. Cao, B. Zheng, W. Shi, J. Yang, Z. Fan, Z. Luo, X. Rui, B. Chen, Q. Yan and H. Zhang, *Adv. Mater.*, 2015, **27**, 4695.
15 S. Mallakpour and E. Khadem, *Chem. Eng. J.*, 2016, **302**, 344.
16 W. Xia, R. Q. Zou, L. An, D. G. Xia and S. J. Guo, *Energy Environ. Sci.*, 2015, **8**, 568.
17 X. Xu, R. Cao, S. Jeong and J. Cho, *Nano Lett.*, 2012, **12**, 4988.
18 M. Zhong, L. Kong, N. Li, Y. Liu, J. Zhu and X. Bu, *Coord. Chem. Rev.*, 2019, **388**, 172.
19 J. Hernandez-Ferrer, A. Anson-Casaos, S. Victor-Roman, A. Santidrian, A. M. Benito and W. K. Maser, *J. Electroanal. Chem.*, 2018, **828**, 86.
20 L. Ma, H. Zhou, Y. Sun, S. Xin, C. Xiao, A. Kumatani, T. Matsue, P. Zhang, S. Ding and F. Li, *Electrochim. Acta*, 2017, **252**, 338.
21 X. Yang, Z. Wen, Z. Wu and X. Luo, *Inorg. Chem. Front.*, 2018, **5**, 687.
22 X. Kang, G. Fu, Z. Song, G. Huo, F. Si, X. Deng, X. Fu and J. Luo, *J. Alloys Compd.*, 2019, **795**, 462.
23 D. Ji, S. Peng, L. Fan, L. Li, X. Qin and S. Ramakrishna, *J. Mater. Chem. A*, 2017, **5**, 23898.
24 R. Liu, J. Duay and S. B. Lee, *ACS Nano*, 2010, **4**, 4299.
25 M. Moussa, G. Shi, H. Wu, Z. Zhao, N. H. Voelcker, D. Losic and J. Ma, *Mater. Des.*, 2017, **125**, 1.
26 M. Lu, Z. Zhang, L. Kang, X. He, Q. Li, J. Sun, R. Jiang, H. Xu, F. Shi, Z. Lei and Z. H. Liu, *J. Mater. Chem. A*, 2019, **7**, 12582.
27 (*a*) D. J. Li, U. N. Maiti, J. Lim, D. S. Choi, W. J. Lee, Y. Oh, G. Y. Lee and S. O. Kim, *Nano Lett.*, 2014, **14**, 1228; (*b*) N. W. Pu, C. Y. Chen, H. X. Qiu, Y. M. Liu, C. H. Song, M. H. Lin and M. D. Ger, *Int. J. Electrochem. Sci.*, 2018, **13**, 6812; (*c*) M. J. Mostazo-Lopez, R. Ruiz-Rosas, A. Castro-Muniz, H. Nishihara, T. Kyotani, E. Morallon and D. Cazorla-Amoros, *Carbon*, 2018, **129**, 510.
28 G. Zhu, H. Wen, M. Ma, W. Wang, L. Yang, L. Wang, X. Shi, X. Cheng, X. Sun and Y. Yao, *Chem. Commun.*, 2018, **54**, 10499.
29 (*a*) I. Nam, N. Kim, G. Kim, J. Park and J. Yi, *J. Power Sources*, 2013, **244**, 56; (*b*) K. Wang, X. Shi, A. Lu, X. Ma, Z. Zhang, Y. Lu and H. Wang, *Dalton Trans.*, 2015, **44**, 151.
30 S. L. Zhang, B. Y. Guan and X. W. Lou, *Small*, 2019, **15**, 13.
31 Y. Zhao, Y. Meng and P. Jiang, *J. Power Sources*, 2014, **259**, 219.
32 Y. Jeon, G. S. Armatas, D. Kim, M. G. Kanatzidis and C. A. Mirkin, *Small*, 2009, **5**, 46.
33 N. Tian, X. Tian, Y. Nie, C. Yang, Z. Zhou and Y. Li, *Chem. Eng. J.*, 2018, **352**, 469.
34 M. Sun, B. Lan, T. Lin, G. Cheng, F. Ye, L. Yu, X. Cheng and X. Zheng, *CrystEngComm*, 2013, **15**, 7010.
35 Y. Wang, Y. Shao, D. W. Matson, J. Li and Y. Lin, *ACS Nano*, 2010, **4**, 1790.
36 D. E. Zhang, J. Y. Gong, J. J. Ma, G. Q. Han and Z. W. Tong, *Dalton Trans.*, 2013, **42**, 16556.
37 J. Chen, X. Wang, X. Cui, G. Yang and W. Zheng, *Chem. Commun.*, 2014, **50**, 557.
38 Z. Chen, X. Peng, X. Zhang, S. Jing, L. Zhong and R. Sun, *Carbohydr. Polym.*, 2017, **170**, 107.
39 J. C. Li, X. P. Qin, P. X. Hou, M. Cheng, C. Shi, C. Liu, H. M. Cheng and M. H. Shao, *Carbon*, 2019, **147**, 303.
40 M. Huang, F. Li, F. Dong, Y. X. Zhang and L. L. Zhang, *J. Mater. Chem. A*, 2015, **3**, 21380.
41 (*a*) D. P. Dubal, D. S. Dhawale, R. R. Salunkhe, S. M. Pawar, V. J. Fulari and C. D. Lokhande, *J. Alloys Compd.*, 2009, **484**, 218; (*b*) B. Wang, J. Park, C. Wang, H. Ahn and G. Wang, *Electrochim. Acta*, 2010, **55**, 6812.
42 M. Fang, X. Tan, M. Liu, S. Kang, X. Hu and L. Zhang, *CrystEngComm*, 2011, **13**, 4915.
43 X. Cui, F. Hu, W. Wei and W. Chen, *Carbon*, 2011, **49**, 1225.
44 K. Wang, X. Ma, Z. Zhang, M. Zheng, Z. Geng and Z. Wang, *Chem. – Eur. J.*, 2013, **19**, 7084.
45 (*a*) Z. Wen, M. Li, S. Zhu and T. Wang, *Int. J. Electrochem. Sci.*, 2016, **11**, 23; (*b*) Z. Wen, M. Li, F. Li, S. Zhu, X. Liu, Y. Zhang, T. Kumeria, D. Losic, Y. Gao, W. Zhang and S. He, *Dalton Trans.*, 2016, **45**, 936.
46 (*a*) D. Gueon and J. H. Moon, *ACS Sustainable Chem. Eng.*, 2017, **5**, 2445; (*b*) D. Hou, H. Tao, X. Zhu and M. Li, *Appl. Surf. Sci.*, 2017, **419**, 580.
47 (*a*) J. Hu, F. Qian, G. Song, W. Li and L. Wang, *Nanoscale Res. Lett.*, 2016, **11**, 469; (*b*) Y. Wu, Y. Ding, T. Hayat, A. Alsaedi and S. Dai, *Appl. Surf. Sci.*, 2018, **459**, 430.
48 B. Liu, Y. Liu, H. Chen, M. Yang and H. Li, *ACS Sustainable Chem. Eng.*, 2019, **7**, 3101.
49 (*a*) S. Qiu, R. Li, Z. Huang, Z. Huang, C. P. Tsui, C. He, X. Han and Y. Yang, *Composites, Part B*, 2019, **161**, 37; (*b*) W. Li, H. Xu, M. Cui, J. Zhao, F. Liu and T. Liu, *Ionics*, 2019, **25**, 999.
50 K. Wang, Z. Wang, X. Wang, X. Zhou, Y. Tao and H. Wu, *J. Power Sources*, 2018, **377**, 44.
51 K. Tao, X. Han, Q. Ma and L. Han, *Dalton Trans.*, 2018, **47**, 3496.
52 H. Li, X. Zhang, R. Ding, L. Qi and H. Wang, *Electrochim. Acta*, 2013, **108**, 497.
53 Z. Li, A. Gu, Z. Lou, J. Sun, Q. Zhou and K. Y. Chan, *J. Mater. Sci.*, 2017, **52**, 4852.
54 J. Zhou, H. Zhao, X. Mu, J. Chen, P. Zhang, Y. Wang, Y. He, Z. Zhang, X. Pan and E. Xie, *Nanoscale*, 2015, **7**, 14697.
55 S. Zhang, D. Li, S. Chen, X. Yang, X. Zhao, Q. Zhao, S. Komarneni and D. Yang, *J. Mater. Chem. A*, 2017, **5**, 12453.

